molecules

MDPI

*Article*

# Bifunctional Hot Water Vapor Template-Mediated Synthesis of Nanostructured Polymeric Carbon Nitride for Efficient Hydrogen Evolution

**Baihua Long [1], Hongmei He [1], Yang Yu [1], Wenwen Cai [1], Quan Gu [2], Jing Yang [3,*] and Sugang Meng [4,*]**

[1] College of Material and Chemical Engineering, Pingxiang University, Pingxiang 337055, China
[2] Key Laboratory of Applied Surface and Colloid Chemistry, Ministry of Education, School of Chemistry and Chemical Engineering, Shaanxi Normal University, Xi'an 710062, China
[3] College of Health Science and Environmental Engineering, Shenzhen Technology University, Shenzhen 518118, China
[4] Key Laboratory of Green and Precise Synthetic Chemistry and Applications, Ministry of Education, Huaibei Normal University, Huaibei 235000, China
* Correspondence: yangjingsztu@163.com (J.Y.); mengsugang@126.com (S.M.); Tel.: +86-18156139968 (S.M.)

**Abstract:** Regulating bulk polymeric carbon nitride (PCN) into nanostructured PCN has long been proven effective in enhancing its photocatalytic activity. However, simplifying the synthesis of nanostructured PCN remains a considerable challenge and has drawn widespread attention. This work reported the one-step green and sustainable synthesis of nanostructured PCN in the direct thermal polymerization of the guanidine thiocyanate precursor via the judicious introduction of hot water vapor's dual function as gas-bubble templates along with a green etching reagent. By optimizing the temperature of the water vapor and polymerization reaction time, the as-prepared nanostructured PCN exhibited a highly boosted visible-light-driven photocatalytic hydrogen evolution activity. The highest $H_2$ evolution rate achieved was 4.81mmol·$g^{-1}$·$h^{-1}$, which is over four times larger than that of the bulk PCN (1.19 mmol·$g^{-1}$·$h^{-1}$) prepared only by thermal polymerization of the guanidine thiocyanate precursor without the assistance of bifunctional hot water vapor. The enhanced photocatalytic activity might be attributed to the enlarged BET specific surface area, increased active site quantity, and highly accelerated photo-excited charge-carrier transfer and separation. Moreover, the sustainability of this environmentally friendly hot water vapor dual-function mediated method was also shown to be versatile in preparing other nanostructured PCN photocatalysts derived from other precursors such as dicyandiamide and melamine. This work is expected to provide a novel pathway for exploring the rational design of nanostructured PCN for highly efficient solar energy conversion.

**Keywords:** carbon nitride; nanostructured; water vapor; $H_2$ evolution



**Citation:** Long, B.; He, H.; Yu, Y.; Cai, W.; Gu, Q.; Yang, J.; Meng, S. Bifunctional Hot Water Vapor Template-Mediated Synthesis of Nanostructured Polymeric Carbon Nitride for Efficient Hydrogen Evolution. *Molecules* **2023**, *28*, 4862. https://doi.org/10.3390/molecules28124862

Academic Editor: Xiaomin Xu

Received: 30 May 2023
Revised: 14 June 2023
Accepted: 18 June 2023
Published: 20 June 2023



## 1. Introduction

The hydrogen evolution via photocatalytic water-splitting is potentially an efficient strategy to store clean energy and alleviate emerging energy issues in the future [1–4]. Polymeric carbon nitride (PCN) has long been proven to exhibit vast potential to achieve this magnificent goal [5–8]. Unfortunately, this stringent goal is greatly hindered by the low efficiency of bulk PCN due to inherent drawbacks, such as inferior separation and transfer for the photoexcited charge carriers, limited visible light absorption, extremely low specific surface area, and finite active sites [9–12]. In this regard, plenty of intelligent strategies have been developed to address the shortcomings mentioned above through the introduction of element doping or functional groups [13–16], modifications with defects or vacancies [17–19], regulating the nanostructure [20–23], adjusting morphology [24–27], or coupling with other semiconductors for heterojunctions and so forth [28–32]. Among these strategies, the nanostructure embedded in the PCN framework was demonstrated to be a

simple and valid method for strikingly promoting the photocatalytic activity of PCN in many aspects [33]. In general, template methods such as hard-templating, soft-templating, and gas-templating were used to create the nanostructures, which resulted in a larger BET specific surface area, more active site quantity and improved the separation efficiency of photo-excited charged carriers.

Among these, the gas-templating method for nanostructure engineering was widely developed because it can circumvent not only the complexity of operations but also the use of extremely toxic chemical reagents that exist in the hard-templating and soft-templating methods. Additionally, this gas-templating method has the advantage of being simple, cost-effective, template-free, and suitable for large-scale synthesis. Normally, the gas-templating approach is primarily classified into two categories. The first is the self-induced gaseous templating method, which engineers the porous structure in PCN by using the self-generated gas as a template. For example, Tang et al. successfully obtained porous PCN with an extraordinary hydrogen evolution rate by direct thermal polymerization of urea at high temperatures in the air without using any additional chemical reagents. The porous structure is created by the emission of a large amount of ammonia gas and water vapor due to the existence of an oxygen element in the urea precursor, which is supposed to act as the gaseous template [34]. In another typical work, Chen et al. created nanoporous PCN with an increased BET specific surface area and pore volume via one-step polymerization of the single urea with self-supported gas, and the resulting nanostructured photocatalyst demonstrated a much higher hydrogen evolution rate [35]. The authors believe that the water vapor bubble served as a gaseous template in the proposed nanoporous PCN. Meanwhile, our groups also developed some simple sulfur-containing organic and inorganic compounds, such as trithiocyanuric acid, thiourea, guanidine thiocyanate, or ammonium thiocyanate, to serve as the unitary precursor for the one-pot production of nanoporous PCN at a high temperature [36–39]. The self-generated sulfur-containing gases produced at high temperatures are thought to be responsible for forming the nanostructure in PCN. However, the above synthesis method needed a high polymerization temperature to produce plenty of gas function as a gaseous template and also induced the destruction of the integrated PCN framework to some extent. The other method uses extra chemical reagents as dynamic gas-bubble templates. To date, specific types of chemical reagents, including $NH_4Cl$, $(NH_4)_2CO_3$, $NaHCO_3$, $(NH_4)_2SO_4$, $(NH_4)_2S_2O_8$ and sublimed sulfur, were intensely used as dynamic gas-bubble templates to promote the formation of nanostructured PCN [40–49]. During high-temperature calcining, the above chemical reagents can thermally decompose into a large number of gases as dynamic bubble templates, whose emissions induce the porous nanostructure in the PCN. Regrettably, the gases ($NH_3$, HCl, and $SO_2$) released by the above thermal decomposition of chemical reagents cannot be reused and are also sometimes detrimental to the environment, even though the method possesses the benefits of being low cost and easy to operate. Therefore, the exploration of green and pollution-free gas-bubble template methods to realize the synthesis of advanced nanostructured PCN is still of great urgency and interest.

Recently, the use of water vapor (completely green and abundant in the earth) for the pretreatment or preparation of the catalyst has been reported, and the as-prepared catalysts show astonishingly enhanced catalytic activity [17,50,51]. For instance, Huang et al. reported that an increase in the grain-boundary density in the $Pd/Al_2O_3$ catalyst is achieved by simple water vapor pretreatment and oxidation. The pretreatment catalyst showed a twelve-fold increase in methane oxidation compared to conventional pretreatments [50]. Yang et al. prepared the few-layered nanostructured PCN by using the bulk PCN and water vapor as the precursor and gas-bubble templates, respectively. The emissions of CO, $H_2$, and NO gas produced from the C/N-steam reforming reactions also played an important role in the formation of nanostructures in the PCN. Thus, the water vapor showed a dual function in their work, one was the dynamic gas-bubble template, and the other was a green initiator reagent for chemical etching [17]. However, their synthesis of nanostructured PCN required high-quality bulk PCN to serve as the precursor, which was relatively complex

and time-consuming, although the method was demonstrated to be facile, green, and easy to scale up.

In this work, we proposed a one-step route for synthesizing nanostructured PCN to efficiently enhance its photocatalytic activity by judiciously introducing hot water vapor into the direct thermal polymerization of the guanidine thiocyanate precursor. The hot water vapor served a dual function as a dynamic gas-bubble template and an assisted chemical etching reagent in this synthesis. In particular, the supply of the water vapor is continuous throughout the whole synthesis procedure. We investigated the effect of the polymerization reaction time and the temperature of the water vapor on the morphology, structure, and optical/photoelectric properties of the as-prepared nanostructured PCN. Benefitting from the synchronous nanostructure and carbon vacancies embedded in the PCN, the optimized water-vapor treatment PCN was four times more effective than that of the bulk PCN treatment for photocatalytic hydrogen evolution. Moreover, this hot water vapor dual-function mediated method was also successfully extended to other PCN precursors (melamine and dicyandiamide) to obtain their corresponding derived nanostructured PCNs. The detailed synthesis processes were described, and comprehensive characterizations were conducted to elucidate the enhanced photocatalytic hydrogen evolution mechanism.

## 2. Results and Discussion

### *2.1. Morphology and Texture*

The nanostructured photocatalysts were prepared via direct thermal polymerization and simultaneous chemical etching of the guanidine thiocyanate precursor with the assistance of $N_2$ flow, carrying the special temperature of the water vapor. We investigated the variability in water-vapor amounts in detail by accurately controlling the temperature of the water vapor and the reaction times during the polymerization process. Unfortunately, the guanidine thiocyanate precursor was burned off at water-vapor temperatures above 60 °C, and thus no photocatalysts were left in our present experimental conditions. The possible explanation is that the PCN or the intermediates of PCN formed during the polymerization process were completely etched by the excess water vapor. In addition, no photocatalysts were collected at the temperature of 60 °C water vapor for 4 h. The above synthesis results suggested that the selection of water vapor temperatures and reaction times is a key factor in providing an optimal amount of water vapor for preparing and modulating the nanostructured PCN.

The changes in the microstructure of the as-prepared photocatalysts were first characterized by SEM and TEM measurements. SEM observations revealed that CGS-CN displayed a compact, thick, and large aggregate morphology (Figure S1). The GS-CN-25 had a similar morphology to that of the CGS-CN due to the insufficient water vapor and short etching reaction time provided in this preparation system. In contrast, both GS-CN-60 and GS-CN-25-4h photocatalysts obtained upon increasing the temperature of the water vapor or prolonging the etching reaction time exhibited looser, thinner, and smaller aggregates. Excitingly, some nanosheets and pores were observed at the surface of the GS-CN-60 photocatalyst, and its contrast also illustrated its maximal BET specific surface area as evidenced by the BET analyses described below. The possible reason for this evolution is due to the significant contribution from the water vapor, which not only avoids the compact and large aggregates of CGS-CN but also its ability to etch the sheets to generate pores via the large number of gases ($H_2$, CO, $CO_2$, and $NH_3$) released during the simultaneous polymerization and etching procedure [51]. In other words, the released gases are able to explode many "tiny bombs" on the thick chunks of the CGS-CN, which leads to the generation of relatively loose, thin, small aggregates and even porous structural characteristics on the GS-CN-60.

TEM results further substantiated this visible evolution, displaying the bulk CGS-CN aggregates' gradual evolution into thin and semitransparent nanosheets along with certain surface pores on the GS-CN-60 photocatalyst by the hot water vapor dual -unction mediated method, as seen in Figure 1a,b. AFM topography and height profiles (Figure 1c–f)

demonstrated that the GS-CN-60 existed as nanosheets with thicknesses ranging from 2 to 6 nm, while the average thickness of the bulk CGS-CN was around 20 nm. The unique morphological characteristics of the GS-CN-x photocatalysts directly affected their textural properties, as evidenced by the BET test.

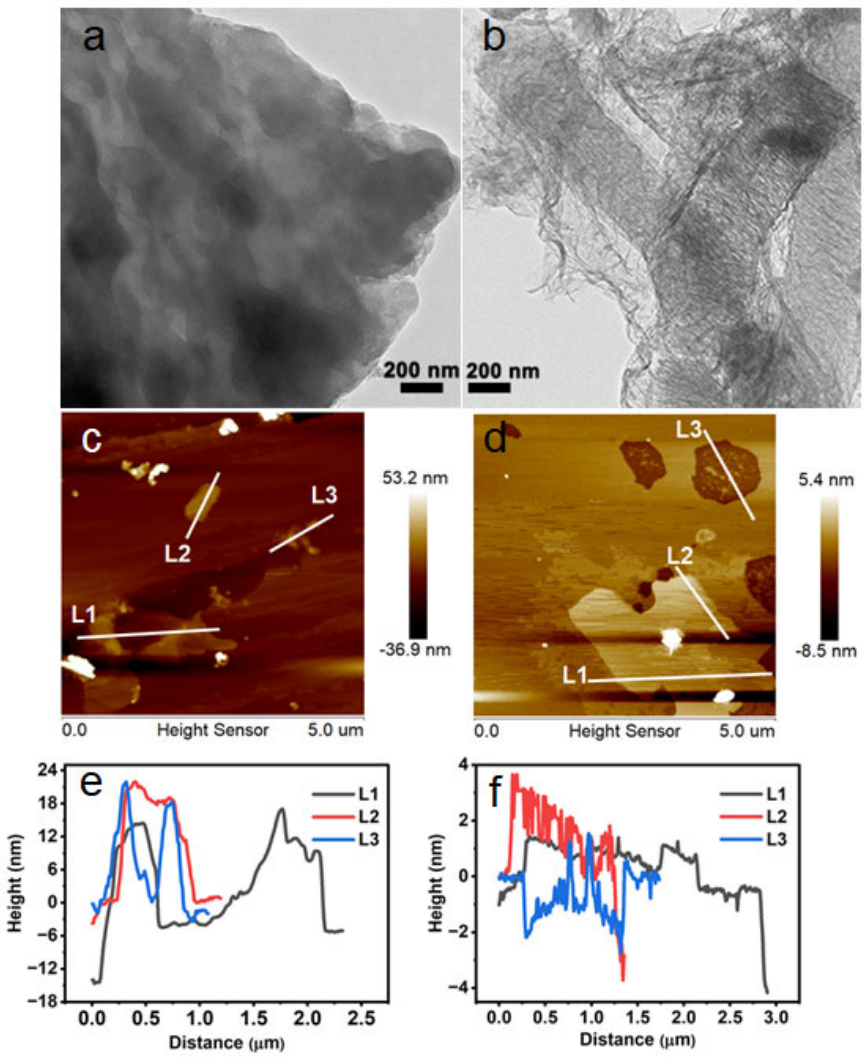


**Figure 1.** TEM images of: (**a**) bulk CGS-CN and (**b**) GS-CN-60. AFM images and corresponding height profile of: (**c**,**e**) bulk CGS-CN; and (**d**,**f**) GS-CN-60 ((**c**,**d**) corresponds to (**e**,**f**), respectively).

BET confirmed that the specific surface area gradually increased from CGS-CN, GS-CN-25, and GS-CN-25-4h to GS-CN-60, as shown in Figure 2. The GS-CN-60 had the largest surface area with 34.1 $m^2 \cdot g^{-1}$, which was about 1.7, 1.9, and 7.1 times higher than those of the GS-CN-25-4h, GS-CN-25, and bulk CGS-CN. Nevertheless, the surface area of GS-CN-25-4h (20.4 $m^2 g^{-1}$) only weakly increased compared to that of the GS-CN-25 (17.9 $m^2 g^{-1}$). These results reflected that the hot water vapor assisted by the dual function mediated strategy exerted the most significant impact on the surface area. Moreover, the adsorption–desorption isothermal curves for GS-CN-x photocatalysts all exhibited typical type IV with an $H_3$-type hysteresis loop and an enlarged pore volume (Figure 2), revealing that they possessed representative porous structural characteristics and were in line with the results of the SEM and TEM images. Consequently, the above results implied that the optimization of the nanostructured PCN with plentiful pores, high specific surface area, and expanded pore volume was successfully prepared by this hot water vapor dual-function mediated strategy by simply adjusting the relative amounts of water vapor, which

promoted the guanidine thiocyanate precursor for suitable seed nucleation, growth, and synchronous etching during the polymerization processes.

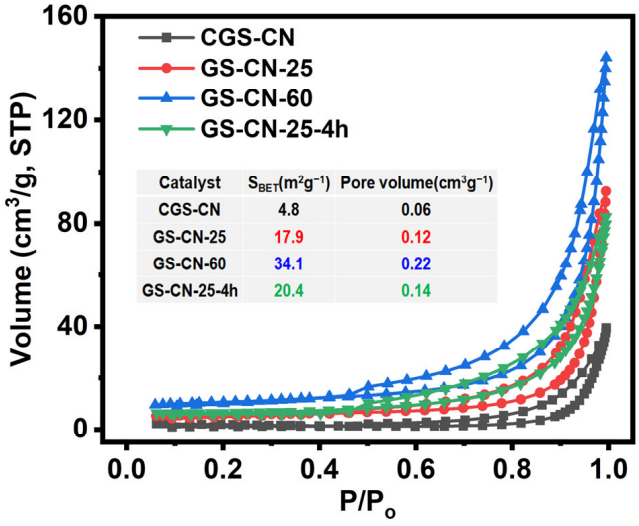


**Figure 2.** $N_2$ adsorption-desorption isotherms of bulk CGS-CN and GS-CN-x photocatalysts.

### *2.2. XRD and FTIR Analysis*

Figure 3a represents the XRD patterns and diffraction peaks of all the photocatalysts. All tested photocatalysts exhibited two distinct diffraction peaks at around 13.3° and 27.2°, which are indexed to the (100) and (002) planes of hexagonal PCN. These reflections correspond to the in-plane structural heptazine units and interlamellar stacking distance, respectively. The results implied that the GS-CN-x could retain the primary heptazine structure of PCN after the water-vapor treatment reaction. Compared with bulk CGS-CN, the (100) diffraction peak intensity for GS-CN-25 showed no noticeable change, indicating that the in-planar layer size of GS-CN-25 had no significant influence (Figure S2). Nonetheless, the GS-CN-60 and GS-CN-25-4h photocatalysts exhibited a slightly weak diffraction peak at (100), attributed to the decrease in-planar layer size. Similarly, the relative intensity of the (002) diffraction peak for GS-CN-60 and GS-CN-25-4h also became weaker, which is attributed to the selective dismemberment of the PCN framework and the formation of the short-range ordered graphite molecular fragments upon increasing the temperature of the water vapor or prolonging the reaction time [52]. In addition, further observation indicated that the (002) peak position for GS-CN-x showed a progressive upshift compared to that of CGS-CN, highlighting the compacted interlayer stacking distance in the resulting water vapor treatment photocatalysts. The reason for this was that the undulated single layers in CGS-CN were planarized by the water-vapor treatment and thus resulted in a tight stack structure for these GS-CN-x photocatalysts [17].

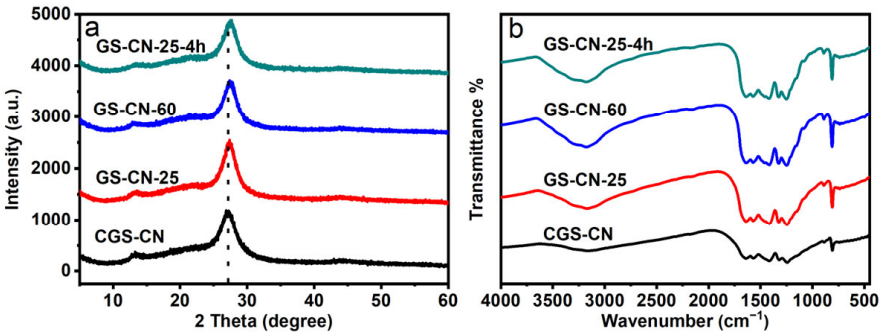


**Figure 3.** (**a**) XRD patterns of bulk CGS-CN and GS-CN-x photocatalysts; and (**b**) FT-IR spectra of bulk CGS-CN and GS-CN-x photocatalysts.

The FT-IR spectra presented in Figure 3b show that the GS-CN-x photocatalysts exhibited the same characteristic vibrational absorption peaks as that of CGS-CN. In any case, the identified peak positions at 810, 1200–1700, and 3000–3500 $cm^{-1}$, respectively, were assigned to the bending vibrations of heptazine units, stretching vibrations of aromatic C-N heterocycles, and stretching vibrations of the -$NH_x$ groups. Interestingly, the more vigorous intensity of these peaks in the region of 3100–3400 $cm^{-1}$ for the GS-CN-x photocatalysts compared with that of the CGS-CN is indicative of more adsorbed $H_2O$ on these GS-CN-x photocatalyst surfaces due to their sizeable open-up surface effects.

### *2.3. XPS and ESR Analysis*

XPS further demonstrated the more subtle chemical structure and valence state of the photocatalysts. The XPS test confirmed the presence of carbon, nitrogen, and oxygen elements for all the photocatalysts, as illustrated in Figure 4a. The C 1s and N 1s high-resolution spectra of the GS-CN-x photocatalysts showed the same binding energies as that of the CGS-CN, indicating that the heptazine structure was hardly changed in the rigid water-vapor treatment conditions. The high-resolution C 1s spectrum revealed two labeled peaks with the binding energy centered at 288.0 and 284.6 eV (Figure 4b), which were assigned to $sp^2$-hybridized aromatic C atoms (N-C=N) in the heptazine rings and adventitious carbon, respectively. The high-resolution N 1s spectrum could be deconvoluted into four labeled peaks with the binding energy positioned at 398.5, 400.1, 401.2, and 404.0 eV, respectively (Figure 4c). The strongest N 1s peak at 398.5 eV corresponded to $sp^2$-hybridized aromatic N atoms (C=N-C) in the heptazine rings. The second strongest N 1s peak at 400.1 eV was indicative of tertiary N atoms from N-$(C)_3$ groups. The third N 1s peak at 401.2 eV was attributed to amino functional groups (C-N-H). The weakest N 1s peak at 404.0 eV was caused by $\pi^*$-excitation. The analysis of the surface C/N atomic ratio results in Table S1 show that these GS-CN-x photocatalysts were deficient in carbon compared to CGS-CN. This result reflected the fact that the carbon vacancies were successfully incorporated into the GS-CN-x framework due to the preferential elimination of carbon atoms in the water-vapor treatment reaction. To distinguish the locations of carbon vacancies in the GS-CN-x framework, the summaries of C and N atomic contents were analyzed and quantified based on the peak area ratio (Figure S3). The atomic percentages of N-$(C)_3$ and C-N-H decreased, and that of C=N-C increased in N 1s XPS spectra for these GS-CN-x photocatalysts as compared with those of the bulk CGS-CN (Figure S3b), indicating that the elimination of the carbon atoms mainly occurred at the N-$(C)_3$ and C-N-H sites to generate carbon vacancies for these GS-CN-x photocatalysts. In addition, the increased atomic percentages of N-C=N in C 1s XPS spectra for GS-CN-x photocatalysts further cross-validate the above-mentioned deduction (Figure S3a). Nonetheless, the decreased atomic percentages of C-C/C=C for GS-CN-x photocatalysts could result from the part of graphitic carbon being removed from the surface by the reductive gas of $H_2$, which was generated through the water vapor etching reaction [51,53].

The direct evidence to confirm the formation of carbon vacancies in GS-CN-x can be further interpreted by EPR. As shown in Figure 4d, the Lorentzian line of bulk CGS-CN showed a feeble signal at g = 2.004. The EPR signal of PCN is stemmed from the unpaired electrons on $sp^2$-C atoms of aromatic C-N heterocycles, which leads to structural defects in the PCN framework. Moreover, the signal intensity increases gradually from CGS-CN, GS-CN-25, and GS-CN-25-4h to GS-CN-60. The increase of unpaired electrons on the $sp^2$-C atoms for GS-CN-x photocatalysts remarkably strengthened the intensity of the Lorentzian line, firmly showing that the concentration of carbon vacancies in the as-prepared GS-CN-x was increased and controllably tuned [54]. However, the bulk C/N atomic ratio in the EA analysis results (Table S2) suggested that the bulk C/N atomic ratio for these GS-CN-x photocatalysts was slightly decreased compared to the bulk CGS-CN, signifying that the carbon vacancies were more likely to be near the surface of the water-vapor-etched photocatalysts.

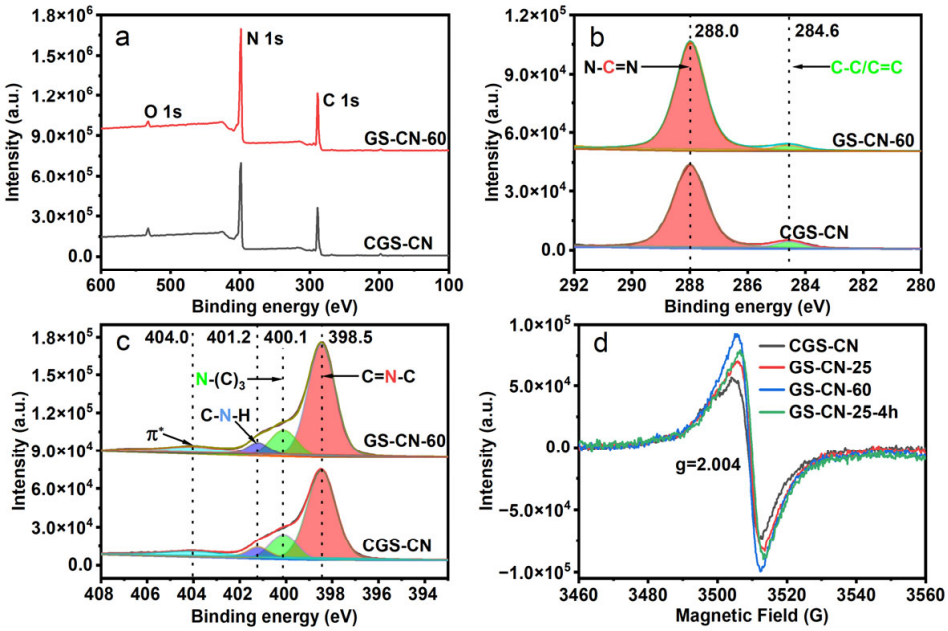


**Figure 4.** XPS patterns of bulk CGS-CN and GS-CN-x photocatalysts: (**a**) survey patterns; (**b**) high-resolution patterns of C1s; (**c**) high-resolution patterns of N1s; and (**d**) room-temperature EPR spectra of bulk CGS-CN and GS-CN-x photocatalysts.

### *2.4. UV-Visible and PL Analysis*

The UV-vis absorption spectra of CGS-CN and GS-CN-x photocatalysts are shown in Figure 5a. The intrinsic absorption edge of the GS-CN-x showed a progressive blue shift compared to that of the bulk CGS-CN, which rendered the enlargement of the intrinsic bandgaps. It is noticeable that GS-CN-60 and GS-CN-25-4h photocatalysts show virtually identical absorption edges and intensities. Furthermore, no evident Urbach tail absorption in the visible-light region for the GS-CN-x was found, indicative of the absence of shallow trap states embedded in the bandgap of GS-CN-x generated by carbon vacancies [18,55]. This also indirectly demonstrated that the following enhancement of GS-CN-x photocatalytic activity was not directly correlated with their optical absorption. The corresponding bandgap energies of the photocatalysts were calculated based on the plots of $[F(R)h\nu]^{1/2}$ versus hν (Figure 5b) and the bandgap energies of CGS-CN (2.56 eV), GS-CN-25 (2.68 eV), GS-CN-60 (2.73 eV), and GS-CN-25-4h (2.73 eV) were estimated. The broadened bandgap for the GS-CN-x catalysts was firmly demonstrated by a similar tendency in the gradual blue shift in the PL emission spectrum (Figure 5c). This hypochromic-shift phenomenon can be well explained as a consequence of the quantum size effect of the nanostructured materials. The values of the valence band were directly determined by XPS valence band spectroscopy (Figure 5d). The band edge of GS-CN-60 (1.97 eV) was revealed as a 0.21 eV negative shift compared to that of CGS-CN (2.18 eV). The conduction band values of CGS-CN and GS-CN-60 could be calculated as −0.38 eV and −0.76 eV, respectively, according to the Equation: $E_{CB} = E_{VB} - E_g$. The corresponding band alignments of CGS-CN and GS-CN-60 are schematically depicted in Figure S4, where the GS-CN-60 exhibited a more thermodynamically enhanced reduction power than that of the CGS-CN, indicative of the more powerful reduction ability of photoexcited electrons at GS-CN-60, which enabled the fast proton reduction in the following photocatalytic hydrogen evolution reaction.

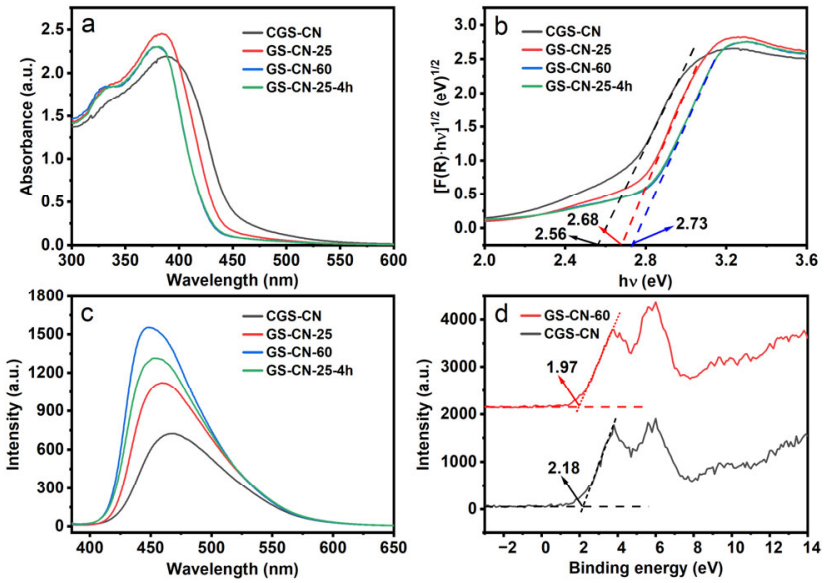


**Figure 5.** (**a**) UV-Vis diffuse reflectance spectra of bulk CGS-CN, GS-CN-x photocatalysts (noted: the nearly same absorption edge and intensity occurred in GS-CN-60 and GS-CN-25-4h); (**b**) The corresponding Kubelka–Munk transformed spectra of bulk CGS-CN and GS-CN-x photocatalysts; (**c**) FL emission spectra of bulk CGS-CN and GS-CN-x photocatalysts; and (**d**) XPS valence-band spectra of bulk CGS-CN and GS-CN-60 photocatalysts.

### *2.5. Time-Resolved PL and Photoelectrochemical Analysis*

To better understand the recombination kinetics of photoexcited charge carriers, the time-resolved PL decay spectra of CGS-CN and GS-CN-x photocatalysts were recorded (Figure 6a). The fitted PL lifetime-decay curves, according to the two-exponential decay model, revealed that the average radiative lifetimes of CGS-CN, GS-CN-25, GS-CN-60, and GS-CN-25-4h were 6.68, 6.31, 5.42, and 5.47 ns, respectively. All the fitting decay parameters and the pertinent details are summarized in Table S3. The shortest lifetime of the singlet exciton in GS-CN-60 clearly implied that its depopulation of the excited states primarily occurred through non-radiative pathways, presumably through charge transfer of the electrons to some favorable carbon defect sites, and then promoted the rapid transfer and separation of charge carriers [56–59]. Concurrently, the change regularity of transient photocurrent responses of the photocatalysts can support the above explanation (Figure 6b). GS-CN-60 gave a higher photocurrent response than those of the other photocatalysts, indicative of its remarkably high charge-carrier separation efficiency. To further understand the dynamic behaviors of photo-generated charge carriers, electrochemical impedance spectroscopy (EIS) was conducted to investigate the properties of the electrode/electrolyte interface, and the result is illustrated in Figure 6c. The GS-CN-60 photocatalyst showed the smallest interfacial charge-transfer resistance due to the synergetic effect of the favorable porous and electronic structures, well in accordance with the photocurrent response. Owning a higher overall electronic conductivity, the photoexcited electron transfer kinetics from the bulk to the interface of GS-CN-60 was faster than that of the other photocatalysts, and therefore it is expected to guarantee high photocatalytic activity.

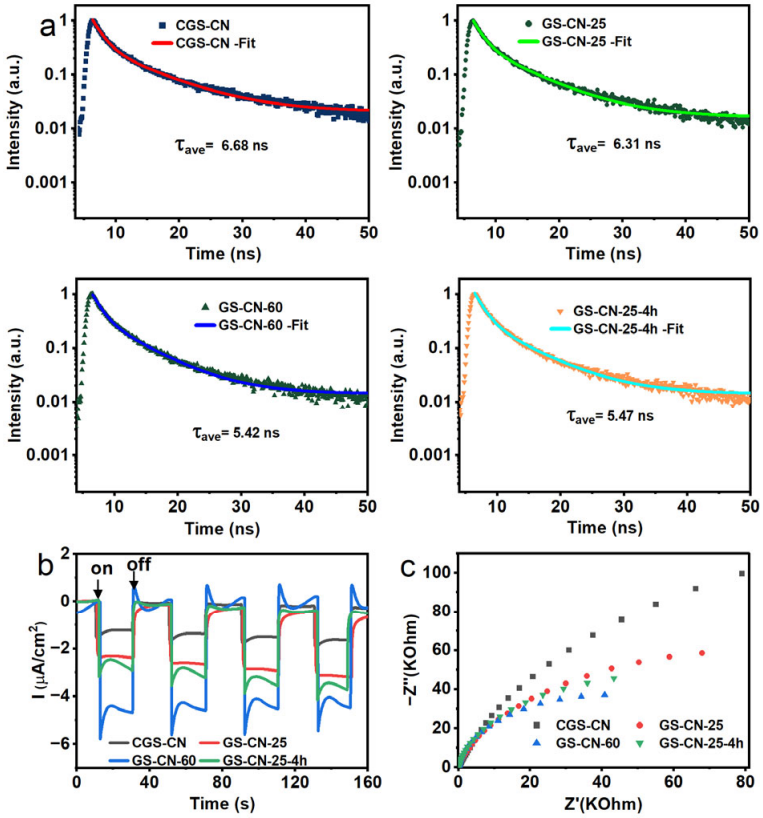


**Figure 6.** (**a**) Time-resolved PL decay spectra of bulk CGS-CN and GSCN-x photocatalysts kinetics monitored at their maximum emission wavelength (CGS-CN: 470 nm; GS-CN-25: 459 nm; GS-CN-60: 448 nm; GS-CN-25-4h: 453 nm) under 365 nm excitation; (**b**) transient photocurrent responses; and (**c**) EIS Nyquist plots of bulk CGS-CN and GS-CN-x photocatalysts.

### *2.6. Photocatalytic Activities*

The photocatalytic activities of the as-prepared photocatalysts were examined by visible-light-induced photocatalytic $H_2$ evolution in coexistence with Pt catalyst and triethanolamine (TEOA) sacrificial electron donor. Initially, we investigated the influence of the concentration of TEOA on the rate of $H_2$ evolution by GS-CN-60 photocatalyst under visible light irradiation. As shown in Figure S5, the $H_2$ evolution rate reached a maximum at a concentration of 10 vol.% TEOA. Hereafter, we chose 10 vol.% TEOA as the sacrificial electron donor for the following experiment. The photocatalytic hydrogen evolution amounts versus irradiation time over the as-prepared photocatalysts were plotted in Figure 7a. The CGS-CN photocatalyst showed the lowest activity, with an $H_2$ evolution rate of 1.19 mmol·h$^{-1}$·g$^{-1}$. As expected, the photocatalytic $H_2$ generation activity was significantly enhanced for the GS-CN-x photocatalysts in comparison with that of CGS-CN, suggesting the positive contribution of the water vapor mediated strategy to the photocatalytic activity. The optimized $H_2$ evolution rate of 4.81 mmol·h$^{-1}$·g$^{-1}$ was achieved for the GS-CN-60 photocatalyst, which was about four times higher than that of the bulk CGS-CN photocatalyst. This result clearly demonstrated the advantage of the hot water vapor treatment to create nanostructures in PCN. At the same time, the high activity was reproducible for the GS-CN-60 photocatalyst, as demonstrated by its excellent long-term stability over a period of 24 h. The generated amount of $H_2$ was about 13.2 mmol·g$^{-1}$ in the first run and could retain the almost equivalent amount of $H_2$ in the subsequent five cycle runs, again revealing the robust stability of the GS-CN-60 for sustainable applications. Above all, the GS-CN-60 maintained a well-retained chemical structure even after five-cycle photocatalytic reactions, as demonstrated in the XRD and FT-IR spectroscopy results, which showed that there was no difference between the used photocatalyst and fresh photocatalyst (Figure S6). The wavelength-dependent apparent quantum yield curve

of GSCN-60 matched well with its UV-Vis absorption spectrum, reflecting the light-induced nature of the reaction. Based on the above discussion, we are now in a position to try to understand the probable mechanisms behind the enhanced photocatalytic $H_2$ evolution activity of GSCN-60. In all, the exceptionally improved photocatalytic activity of GS-CN-60 was due to the synergistic action of high BET specific surface area in contrast to bulk CGS-CN, an enlarged bandgap, outstanding electron reduction ability, and an elevation of the mobility of photo-excited charge carriers. These results, taken together, definitely favored our proceeding with an investigation of the photocatalytic hydrogen evolution reaction.

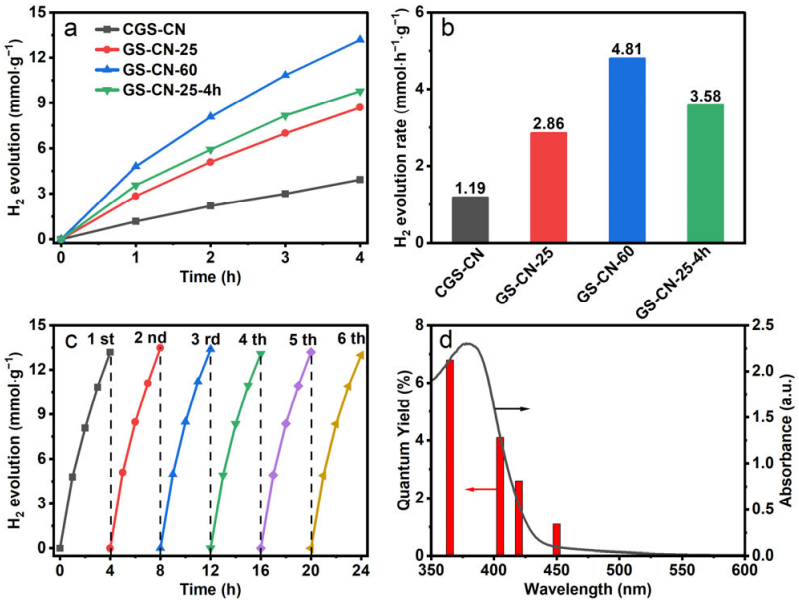


**Figure 7.** (**a**) Time-dependent evolution of $H_2$ produced on bulk CGS-CN and GS-CN-x photocatalysts; (**b**) $H_2$ evolution rate in the first hour on bulk CGS-CN and GS-CN-x photocatalysts; (**c**) recycling test of the GS-CN-60 photocatalyst; and (**d**) M of GS-CN-60 under different wavelengths of monochromatic light.

### *2.7. Photocatalytic Activities of the Other Prepared Nanostructured PCN*

Last but not least, the generality of the effect of hot water vapor with a dual-function mediated strategy was not exclusive to the guanidine thiocyanate precursor. We also verified the effect of the hot water vapor treatment on the other precursors, such as dicyandiamide and melamine. The SEM and TEM results indicated that these water-vapor-treated CDCDA-CN-x and MA-CN-x photocatalysts also showed loose, thin, small aggregates compared with those of the corresponding bulk PCN (Figures S7 and S8), which was well reflected by the gradually increased BET specific surface area results (Table S4). The XRD, FTIR, UV-Visible absorption, and PL spectra of their bulk PCN and corresponding vapor treatment photocatalysts are shown for comparison (Figures S9–S11), indicating that DCDA-CN-x and MA-CN-x showed a similar variation trend with that of the GS-CN-x. These time-resolved PL, photocurrent-response, and EIS-Nyquist characterization results (Figure 8) revealed that these water-vapor-treatment photocatalysts exhibited greatly increased charge separation and electronic conductibility by virtue of their unique porous and electron structures. As expected, the DCDA-CN-x and MA-CN-x displayed obviously enhanced photocatalytic activity.

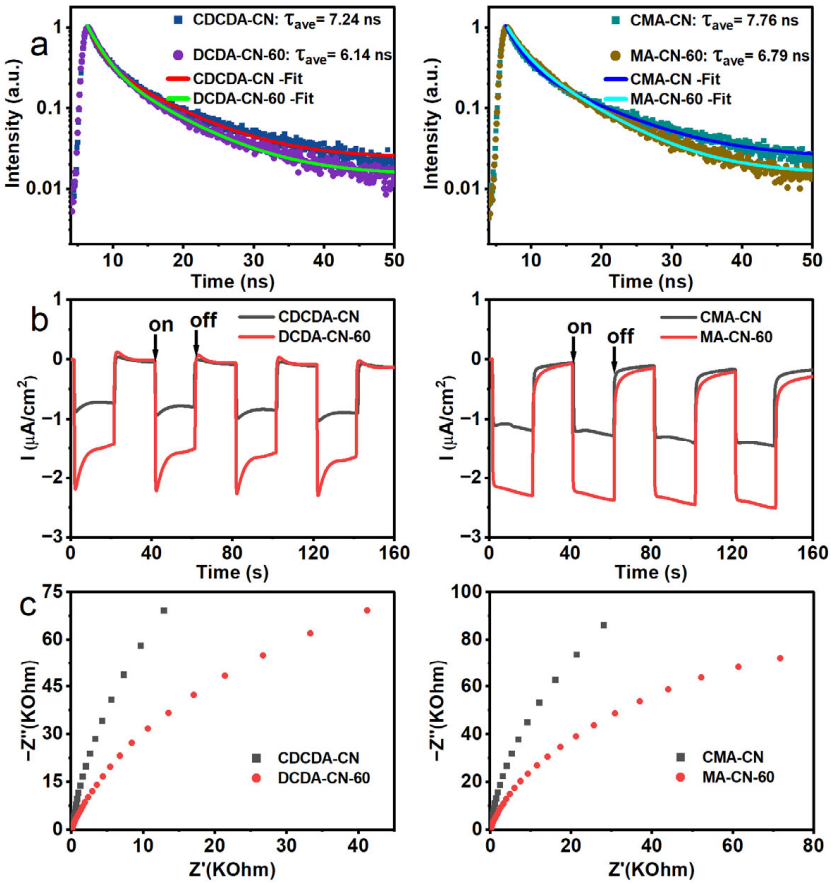


**Figure 8.** (**a**) Time-resolved PL decay spectra of CDCDA-CN, DCDA-CN-60, CMA-CN and MA-CN-60 photocatalysts kinetics monitored at their maximum emission wavelength (CDCDA-CN: 473 nm; DCDA-CN-60: 454 nm; CMA-CN: 473 nm; MA-CN-60: 445 nm) under 365 nm excitation; (**b**) Transient photocurrent responses; and (**c**) EIS Nyquist plots of CDCDA-CN, DCDA-CN-60, CMA-CN and MA-CN-60 photocatalysts.

The hydrogen-evolution rates of the DCDA-CN-60 and MA-CN-60 were 3.8 and 2.7 times higher than those of the bulk CDCDA-CN and CMA-CN, respectively (Figure 9). The difference in exfoliation behavior of PCN from the corresponding different precursors could well account for the different enhanced factors in the photocatalytic activity of $H_2$ evolution.

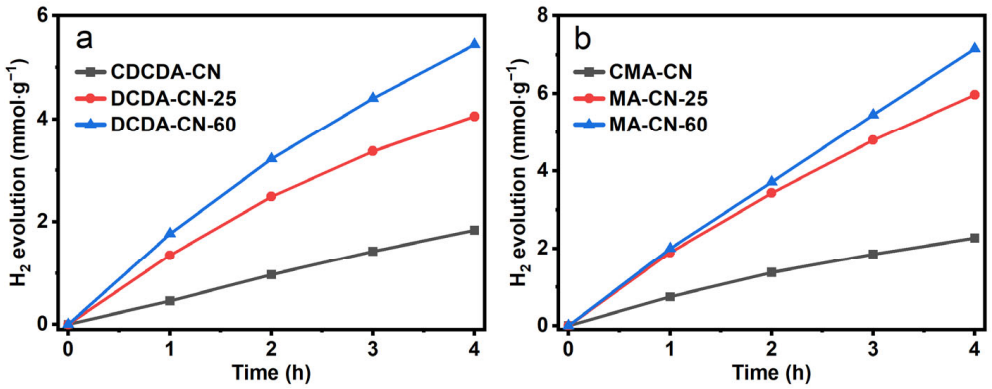


**Figure 9.** Photocatalytic $H_2$ evolution rates of: (**a**) CDCDA-CN and DCDA-CN-x; and (**b**) CMA-CN and MA-CN-x photocatalysts.

## 3. Materials and Methods

### *3.1. Materials*

The guanidine thiocyanate, melamine, dicyandiamide, triethanolamine (TEOA), and $H_2PtCl_6 \cdot 6H_2O$ were of analytical grade and used as received without any further purification. Deionized water was used in all the experiments.

### *3.2. Preparation*

2 g Guanidine thiocyanate was thoroughly ground into tiny powders with an agate mortar. After that, the powders were carefully transferred into a porcelain boat and subsequently heated to 550 °C at 5 °C·min$^{-1}$ with nitrogen flow carrying a specific temperature of water vapor for 2 h in a tubular furnace. To avoid the hot water cooling during the transfer line between the gas-washing bottle and the entrance of the furnace, we twined the heat belt to keep the temperature of the transfer line at 100 °C. During the polymerization process, the hot water vapor, maintained at definite temperatures (25 °C, 60 °C, 80 °C, and 100 °C) via a hotplate magnetic stirrer, was carried into the tubular furnace at the assistance of nitrogen gas with a flow rate of 50 mL/min. Finally, the resulting photocatalysts labeled GS-CN-x (where x represents the temperature of water vapor) were obtained for further use. At the same time, the effect of increasing the water vapor etching reaction time to 4 h for preparing the nanostructure PCN was also explored. The final photocatalyst was denoted as GS-CN-x-y (where x represents the temperature of water vapor, and y represents the reaction time). The schematic diagram of this hot-water-vapor-assisted etching method for nanostructured PCN is illustrated in Scheme S1. In comparison, the preparation of bulk PCN as the control photocatalyst was the same as that of GS-CN-x, except for the absence of hot water vapor, which is denoted as CGS-CN for simplicity.

Similarly, we also used other precursors (melamine and dicyandiamide) to witness the same hot-water-vapor-treatment procedure to prepare their corresponding nanostructured PCN. The resulting photocatalysts were denoted as MA-CN-x (melamine as a precursor) and DCDA-CN-x (dicyandiamide as a precursor), where x still represents the temperature of the water vapor. In the meantime, their corresponding bulk PCN photocatalysts as control photocatalysts were also synthesized via calcining pure melamine and dicyandiamide in the absence of hot water vapor, which were denoted as CMA-CN and CDCDA-CN, respectively.

### *3.3. Characterization*

The scanning emission microscope measurements were conducted using an FEI Nova Nano SEM 230 (Thermo Fisher Scientific, Waltham, MA, USA) Field Emission Scanning Electron Microscope. Transmission electron microscopy (TEM) images were obtained using an FEI Talos (Thermo Fisher Scientific, Waltham, MA, USA) field emission transmission electron microscope. X-ray photoelectron spectroscopy (XPS) data were collected on a Thermo ESCALAB 250 instrument (Thermo Fisher Scientific, Waltham, MA, USA) with a monochromatized Al K$\alpha$ line source (200 W). The Fourier transform infrared (FT-IR) spectra were obtained on a Nicolet Nexus 670 FT-IR spectrometer (Thermo Nicolet Co., Madison, USA) in a range from 4000 to 400 cm$^{-1}$, and the photocatalysts were mixed with KBr at a concentration of ca. 1 wt%. Nitrogen adsorption–desorption experiments were performed at 77 K using Micromeritics Tristar II 3020 equipment (Micromeritics, Norcross, GA, USA). The specific surface area was calculated by the Brunauer-Emmet-Teller (BET) method. Elemental analysis (EA) was carried out on an elemental Analyzer (Elementar vario EL cube, Hanau, Germany). X-ray diffraction (XRD) measurements were performed on a Bruker D8 Advance diffractometer (Bruker, Billerica, MA, USA) with Cu K$\alpha$1 radiation ($\lambda$ = 1.5406 Å). UV-Vis diffuse reflectance spectra (UV-Vis DRS) were collected on Lambda 650s Scan UV-Visible system (Perkin-Elmer, Waltham, MA, USA) using double beam optic, and Teflon was used as the reflectance standard. Electron paramagnetic resonance (EPR) spectra were tested by Bruker model A 300 spectrometer (Bruker, Billerica, MA, USA). The photoluminescence (PL) spectra were done at room temperature on a Hitachi F-7100 type

of spectrophotometer (Hitachi Co., Tokyo, Japan). The time-resolved PL decay spectra were recorded at room temperature on an Edinburgh FI/FSTCSPC FLS-1000 spectrophotometer (Edinburgh, Livingston, UK). The electrochemical measurements were done on a CHI 760E electrochemical workstation (Chenhua Co., Ltd., Shanghai, China) in an electrolytic cell with standard three electrodes. The Ag/AgCl (3M KCl) was used as a reference electrode, and a Pt foil was used as a counter electrode. For the working electrode, the photocatalyst dispersion was dipped into the F-doped tin oxide (FTO) glass with a fixed area of 0.25 $cm^2$ and then dried at 120 °C for 2 h to improve adhesion for further use.

### *3.4. Photocatalytic $H_2$ Evolution Experiments*

The photocatalytic reactions were performed in an 80 mL volume of Schlenk flask at 1 bar atmospheric pressure of Argon. Typically, 10 mg photocatalyst powder as a photosensitizer was ultrasonically dispersed in 10 vol.% TEOA aqueous solution (10 mL), which was used as the sacrificial electron donor. A 3 wt% Pt as the catalyst was loaded onto the surface of the photocatalyst by the photodeposition approach using $H_2PtCl_6 \cdot 6H_2O$. The reaction system was evacuated and then backfilled with the high-purity Argon gas (99.999%). This process was repeated three times to remove air completely, and at the last cycle, the Schlenk flask was backfilled with 1 bar of the high-purity Argon gas before irradiation under a 300 W Xe-lamp with UV cut-off filter ($\lambda > 420$ nm). The temperature of the reaction solution was kept at 25 °C by a flow of cooling water. After irradiation, 0.5 mL of the generated gas was extracted per hour and detected by gas chromatography (Fuli, GC-9790Plus, Wenling, China) equipped with a thermal conductive detector (TCD) using Argon as carrier gas. After four hours of terminating the reaction, the reaction system was repeated to evacuate and backfill the Argon gas for the next cycles of the hydrogen-evolution experiments to verify the stability of the photocatalyst.

The apparent quantum yield ($AQY$) for $H_2$ evolution was measured under a monochromatic light with a bandpass filter of 365, 405, 420, and 450 nm, respectively. The intensity of the light was 140, 127, 107, and 144 $mW \cdot cm^{-2}$ for the 365, 405, 420, and 450 nm monochromatic filters, respectively. The irradiation area was measured as 4.6 $cm^2$. According to the amount of hydrogen produced every hour in the photocatalytic reaction, the $AQY$ was calculated by the Formula (1):

$$AQY = \frac{2 \times M \times N_A}{S \times P \times t \times \lambda/(h \times c)} \quad (1)$$

where $M$ is the mole number of evolved $H_2$ (mol), $N_A$ is Avogadro's constant ($6.022 \times 10^{23}$ $mol^{-1}$), $S$ is the irradiated area ($cm^2$), $P$ is the powder density of irradiation light ($W \cdot cm^{-2}$), $t$ is the irradiation time (s), $\lambda$ is the wavelength of the monochromatic light (nm), $h$ is the Planck constant ($6.626 \times 10^{-34}$ J·s), $c$ is the velocity of light ($3 \times 10^8$ $m \cdot s^{-1}$).

## 4. Conclusions

In summary, nanostructured PCN can be successfully prepared by a green and sustainable water-vapor mediated method through one-pot simultaneous polymerization and chemical etching of the PCN precursors directly with hot water vapor. The nanostructured morphology with carbon vacancies can be created and is controllable by controlling the temperature of the water vapor and the reaction time in the synthesis process. Benefitting from the more exposed surface, increased photo-excited electrons reduction ability, and enhanced photo-excited charge carrier transfer and separation efficiency, the GSCN-60 realized substantially improved photocatalytic hydrogen evolution performance than that of the bulk CGS-CN. The present hot water vapor with a dual-function mediated approach could provide a novel pathway for the preparation of nanostructured PCN materials with high photocatalytic performance.

**Supplementary Materials:** The following supporting information can be downloaded at: https://www.mdpi.com/article/10.3390/molecules28124862/s1, Scheme S1: Proposed one-step synthesis of nanostructured PCN by introducing hot water vapor into the polymerization process of C/N precursors; Figure S1: SEM images of bulk CGS-CN and GS-CN-x photocatalysts; Figure S2: The high-magnification section of the XRD patterns for bulk CGS-CN and GS-CN-x photocatalysts; Figure S3: Summary of C atomic contents in the various photocatalysts determined by C1s spectra (a) and summary of N atomic contents in the various photocatalysts determined by N1s spectra (b); Figure S4: The energy band diagrams of bulk CGS-CN and GS-CN-60; Figure S5: $H_2$ evolution rate from different concentration of TEOA as a sacrificial electron donor by GS-CN-60 photocatalyst. Figure S6: XRD and FT-IR patterns of the GS-CN-60 for photocatalytic $H_2$ evolution before and after five cycling runs; Figure S7: SEM images of CDCDA-CN, DCDA-CN-60, CMA-CN, and MA-CN-60; Figure S8: TEM images of CDCDA-CN, DCDA-CN-60, CMA-CN, and MA-CN-60; Figure S9: XRD patterns of CDCDA-CN and DCDA-CN-x (a), CMA-CN and MA-CN-x (b); Figure S10: FTIR spectra of CDCDA-CN and DCDA-CN-x (a), CMA-CN and MA-CN-x (b); Figure S11: UV-Vis diffuse reflectance spectra (a), the corresponding Kubelka-Munk transformed spectra (b) and PL spectra of CDCDA-CN, DCDA-CN-x, CMA-CN and MA-CN-x (c); Table S1: Surface atomic ratio of all photocatalysts determined by XPS spectra; Table S2: The atom percentage of C, N, O and H atoms in the CGS-CN and GS-CN-60 photocatalysts determined by EA; Table S3: Lifetime and Relative Intensities of the fitting parameters of PL decay curves for CGS-CN and GS-CN-x photocatalysts; Table S4: BET specific surface areas ($S_{BET}$) of the photocatalysts.

**Author Contributions:** B.L.: Conceptualization, data curation, writing—original draft preparation, funding acquisition. H.H.: Investigation, data curation, validation. Y.Y. and W.C.: Investigation, data curation. Q.G.: Formal analysis, writing—review and editing. J.Y. and S.M.: Conceptualization, methodology, supervision, writing—review and editing, funding acquisition. All authors have read and agreed to the published version of the manuscript.

**Funding:** This work is thanks to financial support from the National Natural Science Foundation of China (51563020, 22101186), the Department of Education Project of Jiangxi Province (GJJ2202116), the Natural Science Foundation of Top Talent of SZTU (GDRC202114), the Foundation of Anhui Province for Distinguished Young Scholars (2022AH020038), and the Foundation of State Key Laboratory Incubation Base for Green Processing of Chemical Engineering (KF202201).

**Institutional Review Board Statement:** Not applicable.

**Informed Consent Statement:** Not applicable.

**Data Availability Statement:** Not applicable.

**Conflicts of Interest:** The authors declare no conflict of interest.

**Sample Availability:** Samples of the compounds are available from the authors.

## References

1. Zhou, P.; Navid, I.A.; Ma, Y.; Xiao, Y.; Wang, P.; Ye, Z.; Zhou, B.; Sun, K.; Mi, Z. Solar-to-hydrogen efficiency of more than 9% in photocatalytic water splitting. *Nature* **2023**, *613*, 66–70. [CrossRef] [PubMed]
2. Nishiyama, H.; Yamada, T.; Nakabayashi, M.; Maehara, Y.; Yamaguchi, M.; Kuromiya, Y.; Nagatsuma, Y.; Tokudome, H.; Akiyama, S.; Watanabe, T.; et al. Photocatalytic solar hydrogen production from water on a 100-$m^2$ scale. *Nature* **2021**, *598*, 304–307. [CrossRef]
3. Meng, S.; Chen, C.; Gu, X.; Wu, H.; Meng, Q.; Zhang, J.; Chen, S.; Fu, X.; Liu, D.; Lei, W. Efficient photocatalytic $H_2$ evolution, $CO_2$ reduction and $N_2$ fixation coupled with organic synthesis by cocatalyst and vacancies engineering. *Appl. Catal. B* **2021**, *285*, 119789. [CrossRef]
4. Liu, J.; Liu, Y.; Liu, N.; Han, Y.; Zhang, X.; Huang, H.; Lifshitz, Y.; Lee, S.-T.; Zhong, J.; Kang, Z. Metal-free efficient photocatalyst for stable visible water splitting via a two-electron pathway. *Science* **2015**, *347*, 970–974. [CrossRef] [PubMed]
5. Wang, X.; Maeda, K.; Thomas, A.; Takanabe, K.; Xin, G.; Carlsson, J.M.; Domen, K.; Antonietti, M. A metal-free polymeric photocatalyst for hydrogen production from water under visible light. *Nat. Mater.* **2009**, *8*, 76–80. [CrossRef]
6. Liang, X.; Xue, S.; Yang, C.; Ye, X.; Wang, Y.; Chen, Q.; Lin, W.; Hou, Y.; Zhang, G.; Shalom, M.; et al. The Directional Crystallization Process of Poly (triazine imide) Single Crystals in Molten Salts. *Angew. Chem. Int. Ed.* **2023**, *62*, e202216434. [CrossRef]
7. Rahman, M.Z.; Mullins, C.B. Understanding Charge Transport in Carbon Nitride for Enhanced Photocatalytic Solar Fuel Production. *Acc. Chem. Res.* **2019**, *52*, 248–257. [CrossRef]
8. Ong, W.-J.; Tan, L.-L.; Ng, Y.H.; Yong, S.-T.; Chai, S.-P. Graphitic Carbon Nitride (g-$C_3N_4$)-Based Photocatalysts for Artificial Photosynthesis and Environmental Remediation: Are We a Step Closer to Achieving Sustainability? *Chem. Rev.* **2016**, *116*, 7159–7329. [CrossRef] [PubMed]

9. Lin, L.; Lin, Z.; Zhang, J.; Cai, X.; Lin, W.; Yu, Z.; Wang, X. Molecular-level insights on the reactive facet of carbon nitride single crystals photocatalysing overall water splitting. *Nat. Catal.* **2020**, *3*, 649–655. [CrossRef]
10. Wang, Q.; Li, Y.; Huang, F.; Song, S.; Ai, G.; Xin, X.; Zhao, B.; Zheng, Y.; Zhang, Z. Recent Advances in g-$C_3N_4$-Based Materials and Their Application in Energy and Environmental Sustainability. *Molecules* **2023**, *28*, 432. [CrossRef]
11. Aljuaid, A.; Almehmadi, M.; Alsaiari, A.A.; Allahyani, M.; Abdulaziz, O.; Alsharif, A.; Alsaiari, J.A.; Saih, M.; Alotaibi, R.T.; Khan, I. g-$C_3N_4$ Based Photocatalyst for the Efficient Photodegradation of Toxic Methyl Orange Dye: Recent Modifications and Future Perspectives. *Molecules* **2023**, *28*, 3199. [CrossRef]
12. Cao, D.; Wang, X.; Zhang, H.; Yang, D.; Yin, Z.; Liu, Z.; Lu, C.; Guo, F. Rational Design of Monolithic g-$C_3N_4$ with Floating Network Porous-like Sponge Monolithic Structure for Boosting Photocatalytic Degradation of Tetracycline under Simulated and Natural Sunlight Illumination. *Molecules* **2023**, *28*, 3989. [CrossRef] [PubMed]
13. Patnaik, S.; Sahoo, D.P.; Parida, K. Recent advances in anion doped g-$C_3N_4$ photocatalysts: A review. *Carbon* **2021**, *172*, 682–711. [CrossRef]
14. Kessler, F.K.; Zheng, Y.; Schwarz, D.; Merschjann, C.; Schnick, W.; Wang, X.; Bojdys, M.J. Functional carbon nitride materials-design strategies for electrochemical devices. *Nat. Rev. Mater.* **2017**, *2*, 17030. [CrossRef]
15. Xiao, X.; Gao, Y.; Zhang, L.; Zhang, J.; Zhang, Q.; Li, Q.; Bao, H.; Zhou, J.; Miao, S.; Chen, N.; et al. A Promoted Charge Separation/Transfer System from Cu Single Atoms and $C_3N_4$ Layers for Efficient Photocatalysis. *Adv. Mater.* **2020**, *32*, 2003082. [CrossRef]
16. Lin, J.; Tian, W.; Guan, Z.; Zhang, H.; Duan, X.; Wang, H.; Sun, H.; Fang, Y.; Huang, Y.; Wang, S. Functional Carbon Nitride Materials in Photo-Fenton-Like Catalysis for Environmental Remediation. *Adv. Funct. Mater.* **2022**, *32*, 2201743. [CrossRef]
17. Yang, P.; Ou, H.; Fang, Y.; Wang, X. A Facile Steam Reforming Strategy to Delaminate Layered Carbon Nitride Semiconductors for Photoredox Catalysis. *Angew. Chem. Int. Ed.* **2017**, *56*, 3992–3996. [CrossRef]
18. Yang, P.; Zhuzhang, H.; Wang, R.; Lin, W.; Wang, X. Carbon Vacancies in a Melon Polymeric Matrix Promote Photocatalytic Carbon Dioxide Conversion. *Angew. Chem. Int. Ed.* **2019**, *58*, 1134–1137. [CrossRef]
19. Niu, P.; Yin, L.-C.; Yang, Y.-Q.; Liu, G.; Cheng, H.-M. Increasing the Visible Light Absorption of Graphitic Carbon Nitride (Melon) Photocatalysts by Homogeneous Self-Modification with Nitrogen Vacancies. *Adv. Mater.* **2014**, *26*, 8046–8052. [CrossRef]
20. Talapaneni, S.N.; Singh, G.; Kim, I.Y.; Albahily, K.; Al-Muhtaseb, A.a.H.; Karakoti, A.S.; Tavakkoli, E.; Vinu, A. Nanostructured Carbon Nitrides for $CO_2$ Capture and Conversion. *Adv. Mater.* **2020**, *32*, 1904635. [CrossRef]
21. Tian, N.; Huang, H.; Du, X.; Dong, F.; Zhang, Y. Rational nanostructure design of graphitic carbon nitride for photocatalytic applications. *J. Mater. Chem. A* **2019**, *7*, 11584–11612. [CrossRef]
22. Chen, L.; Song, J. Tailored Graphitic Carbon Nitride Nanostructures: Synthesis, Modification, and Sensing Applications. *Adv. Funct. Mater.* **2017**, *27*, 1702695. [CrossRef]
23. Zheng, Y.; Lin, L.; Wang, X. Nanostructured Carbon Nitrides for Photocatalytic Water Splitting. In *Nanocarbons for Advanced Energy Conversion*, 1st ed.; Feng, X.L., Ed.; Wiley-VCH Verlag GmbH & Co. KGaA: Hoboken, NJ, USA, 2015; pp. 281–300.
24. Thomas, A.; Fischer, A.; Goettmann, F.; Antonietti, M.; Müller, J.-O.; Schlögl, R.; Carlsson, J.M. Graphitic carbon nitride materials: Variation of structure and morphology and their use as metal-free catalysts. *J. Mater. Chem.* **2008**, *18*, 4893–4908. [CrossRef]
25. Kröger, J.; Jiménez-Solano, A.; Savasci, G.; Lau, V.W.H.; Duppel, V.; Moudrakovski, I.; Küster, K.; Scholz, T.; Gouder, A.; Schreiber, M.-L.; et al. Morphology Control in 2D Carbon Nitrides: Impact of Particle Size on Optoelectronic Properties and Photocatalysis. *Adv. Funct. Mater.* **2021**, *31*, 2102468. [CrossRef]
26. Malik, R.; Tomer, V.K. State-of-the-art review of morphological advancements in graphitic carbon nitride (g-CN) for sustainable hydrogen production. *Renew. Sustain. Energy Rev.* **2021**, *135*, 110235. [CrossRef]
27. Long, B.; Zheng, Y.; Lin, L.; Alamry, K.A.; Asiri, A.M.; Wang, X. Cubic mesoporous carbon nitride polymers with large cage-type pores for visible light photocatalysis. *J. Mater. Chem. A* **2017**, *5*, 16179–16188. [CrossRef]
28. Zhang, J.; Liang, X.; Zhang, C.; Lin, L.; Xing, W.; Yu, Z.; Zhang, G.; Wang, X. Improved Charge Separation in Poly(heptazine-triazine) Imides with Semi-coherent Interfaces for Photocatalytic Hydrogen Evolution. *Angew. Chem. Int. Ed.* **2022**, *61*, e202210849.
29. Huang, D.; Yan, X.; Yan, M.; Zeng, G.; Zhou, C.; Wan, J.; Cheng, M.; Xue, W. Graphitic Carbon Nitride-Based Heterojunction Photoactive Nanocomposites: Applications and Mechanism Insight. *ACS Appl. Mater. Interfaces* **2018**, *10*, 21035–21055. [CrossRef]
30. Zhang, J.; Zhang, M.; Sun, R.-Q.; Wang, X. A Facile Band Alignment of Polymeric Carbon Nitride Semiconductors to Construct Isotype Heterojunctions. *Angew. Chem. Int. Ed.* **2012**, *51*, 10145–10149. [CrossRef]
31. Jiang, Z.; Wan, W.; Li, H.; Yuan, S.; Zhao, H.; Wong, P.K. A Hierarchical Z-Scheme α-$Fe_2O_3$/g-$C_3N_4$ Hybrid for Enhanced Photocatalytic $CO_2$ Reduction. *Adv. Mater.* **2018**, *30*, 1706108. [CrossRef]
32. Chen, S.; Wei, J.; Ren, X.; Song, K.; Sun, J.; Bai, F.; Tian, S. Recent Progress in Porphyrin/g-$C_3N_4$ Composite Photocatalysts for Solar Energy Utilization and Conversion. *Molecules* **2023**, *28*, 4283. [CrossRef]
33. Iqbal, W.; Yang, B.; Zhao, X.; Rauf, M.; Waqas, M.; Gong, Y.; Zhang, J.; Mao, Y. Controllable synthesis of graphitic carbon nitride nanomaterials for solar energy conversion and environmental remediation: The road travelled and the way forward. *Catal. Sci. Technol.* **2018**, *8*, 4576–4599. [CrossRef]
34. Martin, D.J.; Qiu, K.; Shevlin, S.A.; Handoko, A.D.; Chen, X.; Guo, Z.; Tang, J. Highly Efficient Photocatalytic $H_2$ Evolution from Water using Visible Light and Structure-Controlled Graphitic Carbon Nitride. *Angew. Chem. Int. Ed.* **2014**, *53*, 9240–9245. [CrossRef]

35. Zhang, Y.; Liu, J.; Wu, G.; Chen, W. Porous graphitic carbon nitride synthesized via direct polymerization of urea for efficient sunlight-driven photocatalytic hydrogen production. *Nanoscale* **2012**, *4*, 5300–5303. [CrossRef] [PubMed]
36. Zhang, J.; Sun, J.; Maeda, K.; Domen, K.; Liu, P.; Antonietti, M.; Fu, X.; Wang, X. Sulfur-mediated synthesis of carbon nitride: Band-gap engineering and improved functions for photocatalysis. *Energy Environ. Sci.* **2011**, *4*, 675–678. [CrossRef]
37. Zhang, G.; Zhang, J.; Zhang, M.; Wang, X. Polycondensation of thiourea into carbon nitride semiconductors as visible light photocatalysts. *J. Mater. Chem.* **2012**, *22*, 8083–8091. [CrossRef]
38. Long, B.; Lin, J.; Wang, X. Thermally-induced desulfurization and conversion of guanidine thiocyanate into graphitic carbon nitride catalysts for hydrogen photosynthesis. *J. Mater. Chem. A* **2014**, *2*, 2942–2951. [CrossRef]
39. Cui, Y.; Wang, Y.; Wang, H.; Cao, F.; Chen, F. Polycondensation of ammonium thiocyanate into novel porous g-$C_3N_4$ nanosheets as photocatalysts for enhanced hydrogen evolution under visible light irradiation. *Chin. J. Catal.* **2016**, *37*, 1899–1906. [CrossRef]
40. Madhurima, V.P.; Kumari, K.; Jain, P.K. A facile single-step approach to achieve in situ expanded g-$C_3N_4$ for improved photodegradation performance. *Polym. Adv. Technol.* **2023**, *34*, 578–586. [CrossRef]
41. Kamal Hussien, M.; Sabbah, A.; Qorbani, M.; Hammad Elsayed, M.; Raghunath, P.; Lin, T.-Y.; Quadir, S.; Wang, H.-Y.; Wu, H.-L.; Tzou, D.-L.M.; et al. Metal-free four-in-one modification of g-$C_3N_4$ for superior photocatalytic $CO_2$ reduction and $H_2$ evolution. *Chem. Eng. J.* **2022**, *430*, 132853. [CrossRef]
42. Khedr, T.M.; El-Sheikh, S.M.; Endo-Kimura, M.; Wang, K.; Ohtani, B.; Kowalska, E. Development of Sulfur-Doped Graphitic Carbon Nitride for Hydrogen Evolution under Visible-Light Irradiation. *Nanomaterials* **2023**, *13*, 62. [CrossRef]
43. Yu, S.; Li, C.; Wu, H.; Wang, Y.; Wang, L.; Dong, H.; Han, Z. Ultrathin Mesoporous Carbon Nitride Nanosheets Prepared Through a One-Pot Approach towards Enhanced Photocatalytic Activity. *Energy Technol.* **2020**, *8*, 2000719. [CrossRef]
44. Wang, C.; Zhang, G.; Zhang, H.; Li, Z.; Wen, Y. One-pot synthesis of porous g-$C_3N_4$ nanosheets with enhanced photocatalytic activity under visible light. *Diam. Relat. Mater.* **2021**, *116*, 108416. [CrossRef]
45. He, F.; Chen, G.; Yu, Y.; Zhou, Y.; Zheng, Y.; Hao, S. The sulfur-bubble template-mediated synthesis of uniform porous g-$C_3N_4$ with superior photocatalytic performance. *Chem. Commun.* **2015**, *51*, 425–427. [CrossRef]
46. Zhang, J.; Zhang, M.; Zhang, G.; Wang, X. Synthesis of Carbon Nitride Semiconductors in Sulfur Flux for Water Photoredox Catalysis. *ACS Catal.* **2012**, *2*, 940–948. [CrossRef]
47. Zhang, D.; Guo, Y.; Zhao, Z. Porous defect-modified graphitic carbon nitride via a facile one-step approach with significantly enhanced photocatalytic hydrogen evolution under visible light irradiation. *Appl. Catal. B* **2018**, *226*, 1–9. [CrossRef]
48. Wu, X.; Ma, H.; Zhong, W.; Fan, J.; Yu, H. Porous crystalline g-$C_3N_4$: Bifunctional $NaHCO_3$ template-mediated synthesis and improved photocatalytic $H_2$-evolution rate. *Appl. Catal. B* **2020**, *271*, 118899. [CrossRef]
49. Jiang, Y.; Sun, Z.; Tang, C.; Zhou, Y.; Zeng, L.; Huang, L. Enhancement of photocatalytic hydrogen evolution activity of porous oxygen doped g-$C_3N_4$ with nitrogen defects induced by changing electron transition. *Appl. Catal. B* **2019**, *240*, 30–38. [CrossRef]
50. Huang, W.; Johnston-Peck, A.C.; Wolter, T.; Yang, W.-C.D.; Xu, L.; Oh, J.; Reeves, B.A.; Zhou, C.; Holtz, M.E.; Herzing, A.A.; et al. Steam-created grain boundaries for methane C-H activation in palladium catalysts. *Science* **2021**, *373*, 1518–1523. [CrossRef]
51. Long, B.; Yan, G.; He, H.; Meng, S. Porous and Few-Layer Carbon Nitride Nanosheets via Surface Steam Etching for Enhanced Photodegradation Activity. *ACS Appl. Nano Mater.* **2022**, *5*, 7798–7810. [CrossRef]
52. Gao, S.; Wang, X.; Song, C.; Zhou, S.; Yang, F.; Kong, Y. Engineering carbon-defects on ultrathin g-$C_3N_4$ allows one-pot output and dramatically boosts photoredox catalytic activity. *Appl. Catal. B* **2021**, *295*, 120272. [CrossRef]
53. Tay, Q.; Kanhere, P.; Ng, C.F.; Chen, S.; Chakraborty, S.; Huan, A.C.H.; Sum, T.C.; Ahuja, R.; Chen, Z. Defect Engineered g-$C_3N_4$ for Efficient Visible Light Photocatalytic Hydrogen Production. *Chem. Mater.* **2015**, *27*, 4930–4933. [CrossRef]
54. Wang, X.; Meng, J.; Zhang, X.; Liu, Y.; Ren, M.; Yang, Y.; Guo, Y. Controllable Approach to Carbon-Deficient and Oxygen-Doped Graphitic Carbon Nitride: Robust Photocatalyst Against Recalcitrant Organic Pollutants and the Mechanism Insight. *Adv. Funct. Mater.* **2021**, *31*, 2010763. [CrossRef]
55. Wang, X.; Xia, Y.; Wang, H.; Jiao, X.; Chen, D. Etching-induced highly porous polymeric carbon nitride with enhanced photocatalytic hydrogen evolution. *Chem. Commun.* **2021**, *57*, 4138–4141. [CrossRef]
56. Guo, Y.; Li, J.; Yuan, Y.; Li, L.; Zhang, M.; Zhou, C.; Lin, Z. A Rapid Microwave-Assisted Thermolysis Route to Highly Crystalline Carbon Nitrides for Efficient Hydrogen Generation. *Angew. Chem. Int. Ed.* **2016**, *55*, 14693–14697. [CrossRef]
57. Shi, L.; Yang, L.; Zhou, W.; Liu, Y.; Yin, L.; Hai, X.; Song, H.; Ye, J. Photoassisted Construction of Holey Defective g-$C_3N_4$ Photocatalysts for Efficient Visible-Light-Driven $H_2O_2$ Production. *Small* **2018**, *14*, 1703142. [CrossRef] [PubMed]
58. Li, F.; Yue, X.; Zhang, D.; Fan, J.; Xiang, Q. Targeted regulation of exciton dissociation in graphitic carbon nitride by vacancy modification for efficient photocatalytic $CO_2$ reduction. *Appl. Catal. B* **2021**, *292*, 120179. [CrossRef]
59. Zhang, G.; Li, G.; Lan, Z.-A.; Lin, L.; Savateev, A.; Heil, T.; Zafeiratos, S.; Wang, X.; Antonietti, M. Optimizing Optical Absorption, Exciton Dissociation, and Charge Transfer of a Polymeric Carbon Nitride with Ultrahigh Solar Hydrogen Production Activity. *Angew. Chem. Int. Ed.* **2017**, *56*, 13445–13449. [CrossRef]